Metallic Multi-Material Adhesive Joint Testing and Modeling for Vehicle Lightweighting

Brock Watson[a], Yogesh Nandwani[a], Michael J Worswick[a], Duane S Cronin[a]

[a]Department of Mechanical and Mechatronics Engineering, University of Waterloo,
200 University Avenue West, Waterloo, Ontario, Canada
bwatson@uwaterloo.ca, ynandwan@uwaterloo.ca,
michael.worswick@uwaterloo.ca, duane.cronin@uwaterloo.ca

Abstract

While adhesive bonding has been shown to be a beneficial technique to join multi-material automotive bodies-in-white, quantitatively assessing the effect of adherend response on the ultimate strength of adhesively bonded joints is necessary for accurate joint design.

In the current study, thin adherend single lap shear testing was carried out using three sheet metals used to replace mild steel when lightweighting automotive structures: hot stamped Usibor® 1500 AS ultra-high strength steel (UHSS), aluminum (AA5182), and magnesium (ZEK 100). Six combinations of single and multi-material samples were bonded with a one-part toughed structural epoxy adhesive and experimentally tested to measure the force, displacement across the bond line, and joint rotation during loading. Finite element models of each test were analyzed using LS-DYNA to quantitatively assess the effects of the mode mixity on ultimate joint failure. The adherends were modeled with shell elements and a cohesive zone model was implemented using bulk material properties for the adhesive to allow full three-dimensional analysis of the test, while still being computationally efficient.

The UHSS-UHSS joint strength (27.2 MPa; SD 0.6 MPa) was significantly higher than all other material combinations, with joint strengths between 17.9 MPa (SD 0.9 MPa) and 23.9 MPa (SD 1.4 MPa). The models predicted the test response (average R^2 of 0.86) including the bending deformation of the adherends, which led to mixed mode loading of the adhesive. The critical cohesive element in the UHSS-UHSS simulation predicted 85% Mode II loading at failure while the other material combinations predicted between 41% and 53% Mode II loading at failure, explaining the higher failure strength in the UHSS-UHSS joint.

This study presents a computational method to predict adhesive joint response and failure in multi-material structures, and highlights the importance of the adherend bending stiffness and on joint rotation and ultimate joint strength.

Keywords: metals, hybrid joints, toughened adhesives, finite element stress analysis, vehicle lightweighting

1 Introduction

With ever-increasing demands to reduce vehicle emissions, increase fuel economy, and extend the range of electric vehicles, the necessity to reduce vehicle weight is also increasing. According to Mayyas *et al*. [1], the body in white (BIW) of a typical sedan accounts for 20% to 25% of a vehicle's total mass, and, in a

high production volume vehicle, is usually made of thin steel structures spot-welded together. A case study by Conklin *et al*. [2] on the reduction of the mass of the BIW of a midsized high volume production vehicle strategically integrated high strength steel and aluminum components to reduce the original mass of the BIW from 315 kg to 231 kg, a 27% reduction. This study demonstrated the potential of multi-material structures to drastically reduce vehicle mass. A difficulty acknowledged by Peroni *et al*. [3] in creating multi-material structures is joining dissimilar metals and ensuring structural integrity once joined, which is critical to maintaining the crashworthiness of a well-designed structure.

Traditional methods of joining automotive bodies-in-white, such as resistance spot welding, can cause challenges when attempting to join dissimilar metals due to the formation of embrittling intermetallic compounds during welding. When joining multi-material structures together, non-traditional joining techniques are required, such as the use of a weldable element between the two dissimilar metals, mechanical fasteners or adhesive bonding as demonstrated in a study by Meschut *et al*. [4].

The single lap shear test (*e.g.* ASTM D 3156-07) with thin adherends (1 mm to 2 mm) can be used to determine comparative strengths of various adhesive-adherend combinations, to compare various bonding processes, and to monitor the quality of materials and bonding processes. When this sample is loaded, a moment is generated at the bond interface due to the offset of the adherends corresponding to the thickness of the adhesive and half thicknesses of the adherends. This moment leads to bending of the adherends that can be observed as rotation of the joint relative to the load path. While the intended primary mode of loading in this type of testing is shear (Mode II), the bending of the adherends induces normal (Mode I) loading, leading to a mixed-mode stress state at the ends of the bond line, as noted by Gonçalves *et al*. [5]. This bending can be reduced, if desired, by using thicker adherends (*e.g.* 9.53 mm) as suggested by ASTM D 5656-10; however, these thicker adherends fall outside acceptable sheet metal thicknesses used in an automotive BIW (roughly 0.5 mm to 5 mm, as reported by Matsuyama & Yamashita [6]) and are thus more conducive to adhesive characterization rather than joint characterization.

Previous studies on adhesive testing using the single lap shear specimen with mixed adherend materials have been carried out by Banea *et al*. [7] who focused on aluminum and high-strength steel (HSS) to carbon fiber reinforced polymer (CFRP) joints, Hua *et al*. [8] who studied titanium to CFRP joints, Avendano *et al*. [9] who investigated polymer to CFRP joints, and Ghosh *et al*. [10] who studied steel to polymer joints. Of the studies in which both multi-material and single material joints were investigated, Ghosh *et al.* found that steel-steel samples had roughly ten times the strength to failure (12.65 MPa) compared to steel-polypropylene (1.22 MPa) and polypropylene-polypropylene (0.97 MPa) adherend samples. Banea *et al*. found that for short lap lengths (12.5 mm) there was little difference in the peak strength between CFRP-CFRP, HSS-HSS and CFRP-HSS combinations, but that for longer overlap lengths (25 mm and 50 mm), the multi-material joints tended perform 20% to 25% worse when compared to the CFRP-CFRP tests. These studies demonstrated that a wide range of joint strength can be measured using the same bond area and adhesive by changing the adherends, but did not generally focus on metals commonly used in the automotive industry for light-weighting applications, such as high strength steel, aluminum and magnesium. In a study by Kafkalidis & Thouless [11] in which dissimilar thickness adherends were tested,

larger differences in thickness tended to decrease the joint strength due to increasing the eccentricity of loading, which induced larger bending moments in the bond line.

A number of researchers have applied finite element modeling techniques to model the thin-adherend single lap shear test. These models are typically two-dimensional with small plane strain or plane stress elements used to model the adherends and a cohesive zone model (CZM) mesh (as shown by Kafkalidis & Thouless [11]) or planar element mesh to represent the adhesive (as demonstrated by Guess *et al*. [12]). In an early study using finite element modeling to investigate the single lap shear test, Richardson *et al.* [13] noted that the plane strain assumption was valid for the adherend near the centerline of the samples, while a plane stress condition was appropriate close to the edge. The authors also noted that the adhesive was in the plane strain condition for a larger portion of the width of the sample compared to the adherends. These plane strain and plane stress considerations may be further complicated in multi-material lap shear tests, in which the adherends exhibit different out of plane behaviors due to Poisson's effects. Models using hexahedral solid elements have also been used to model the single lap shear test; however, these models also required very fine mesh densities as demonstrated by Hua *et al*. [8]. The ability to transfer these fine mesh modeling techniques to larger scale impact analyses is currently somewhat limited because the computational cost associated with the fine mesh and transferring to full three dimensions from the planar case is prohibitively computationally expensive for all but the simplest analysis.

The current study focuses on the response of multi-material adhesive joints to lap shear-loading conditions. Of particular interest, dissimilar metallic joints are considered, as opposed to metal-composite joints [7-10] that are more commonly found in the literature, considering a range of adherend alloys and strengths including hot stamped ultra high strength steel (Usibor® 1500-AS) and lower density aluminum (AA5182) and magnesium (ZEK100) alloys. These alloys are candidate substitutes for mild steel to reduce weight in automotive structures and body panels. Future multi-material vehicle architectures mandate adoption of multi-material metallic joints; hence, the need to understand the performance of such joints made using techniques considered compatible with automotive adhesive joining practice. A numerical modelling framework is adopted to predict adhesive failure using cohesive zone treatment of the adhesive and shell elements for the adherend materials that is also compatible with current automotive crashworthiness simulation practice. A key distinction in the current approach is the fundamental characterization of the adhesive properties using bulk adhesive testing as opposed to more commonly employed inverse modelling approaches. In the experiments, global load-displacement measures as well as local measures of joint kinematics (rotation) are used to assess the resulting predictions of joint response and failure, including identification of the role of differences in adherend strength and stiffness in altering mode mixity within the current multi-material joints.

2 Test and Modelling Methodology

Single lap shear adhesive testing was carried out to assess the response of various combinations of metallic adherends bonded with a commercially-available structural adhesive. Specifically, combinations of a fully martensitic Usibor® 1500-AS ultra-high strength steel (UHSS), an O temper 5xxx series aluminum alloy (Al-5182), and a fully annealed rare earth magnesium alloy (ZEK 100) were bonded with a one-part

toughened epoxy adhesive (3M™ SA9850, 3M Canada Company, London, Ontario, Canada) and tested. Given the focus on automotive-compatible adhesive joining practice, the same adhesive, joint preparation and cure cycle was used for each joint configuration (material combination) considered. Finite element models of these lap shear tests were created to model these multi-material joints to provide insight for the use of these adherend combinations in larger, more complicated structures.

2.1 Multi-Material Single Lap Shear Testing

The lap shear tests were carried out using a test specimen similar to that described in ASTM D 3165-07 (Figure 1). The distance between the lap joint and the backing adherend of the specimen (labeled 'Gap' in Figure 1) was larger than suggested in ASTM D 3165-07 to further induce bending of the adherends, which ultimately led to mixed mode loading of the adhesive prior to failure. For all tests, the bond line thickness was 0.007" (0.18 mm) as recommended by the adhesive manufacturer.

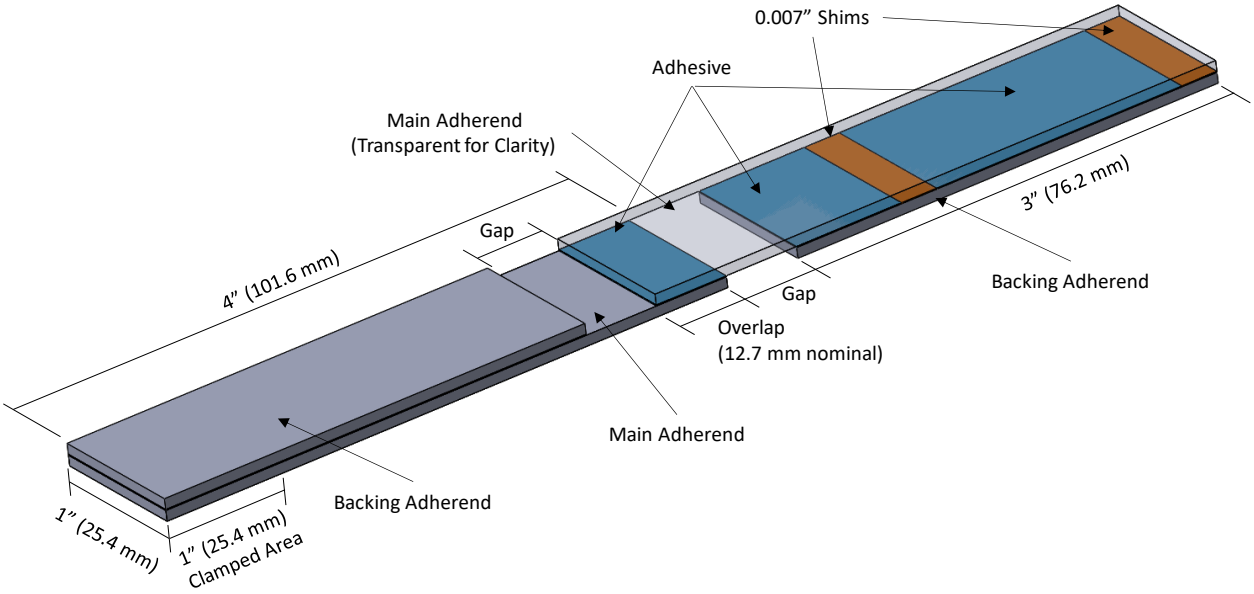

Figure 1: Geometry of single lap shear test samples

After the aluminum and magnesium adherends were cut from sheet material, the surfaces were cleaned with methyl ethyl ketone (MEK) to remove any potential contaminates. The UHSS used in this study was a press hardened steel processed using the parameters discussed by Omer *et al*. [14]. This steel had an aluminum-silicon coating for corrosion protection and prevention of iron oxide scale which is converted into an aluminum-silicon-iron intermetallic coating during heating and hot forming. The coating was not removed or modified prior to testing, though, as with the aluminum and magnesium alloys, the surface of the as-formed steel was cleaned with MEK immediately prior to bonding. The UHSS adherends used in this study were cut from hot-formed hat sections. The first step in the forming process was to austenitize the blank in an oven at 930 °C for 6 min. Following austenitizing, the blank was transferred to a room temperature die where the blank was simultaneously formed and quenched at a rate above 30 °C/s to

form a fully martensitic steel microstructure. The hat sections were then allowed to air cool after removal from the die. Finally, the single lap shear adherends were water jet cut from the side wall of the formed components. The nominal thickness of the magnesium and aluminum adherends was 0.065" (1.65 mm) while the steel adherends were 0.071" (1.8 mm).

Lap shear samples were created for all three adherend metals (*i.e.* steel-steel, aluminum-aluminum, and magnesium-magnesium) as well as the combinations of all three metals (*i.e.* steel-aluminum, steel-magnesium, and aluminum-magnesium). Three samples were tested for each adherend-adhesive combination (6 adherend-adhesive combinations, 18 samples in total). The samples were assembled and held in place between two pieces of float glass while curing according to the manufacturer's recommendations (60 min at 170 ^{o}C). After curing, the spew fillets at the root of the bond lines were removed to ensure a flat, square surface of the adhesive relative to the adherend. After the removal of the spew fillets, the overlap length of each sample was measured to allow for the calculation of the nominal failure stress of each sample after testing.

The samples were tested using a custom-made hydraulic load frame with a 101.6 mm (4") bore x 152.4 mm (6") stroke hydraulic cylinder (Parker Cylinder Division; Owen Sound, Ontario, Canada) controlled using an MTS 407 hydraulic controller (MTS 407; Eden Prairie, Minnesota, USA). The test force was measured using a 90 kN (20 000 lb) loadcell (Transducer Techniques SWP 20k; Temecula, California, USA) and the cylinder displacement was measured with a cylinder mounted linear variable differential transformer (LVDT). The data was acquired using a National Instruments Daqpad-6015 DAC system and Labview 7.1 software. Each test was also recorded at resolution of 1920 x 1080 pixels (approximately 0.015 mm/pixel in the area of interest) and 30 fps using a single, high-resolution DSLR camera (Nikon D3200; Tokyo, Japan) fitted with a 105 mm f2.8 macro lens. The samples were tested at room temperature with a constant crosshead velocity of 0.18 mm/s (corresponding to a nominal shear strain rate of 1.0 s^{-1} for the bond line thickness tested) as measured by the LVDT.

To provide additional data with which to compare the model, the displacement of the backing plates relative to each other (change in distance between Point 'A' and Point 'B' in Figure 2) and the rotation of the bond line (change in angle of the line segment 'C-D' in Figure 2) were measured using tacking software originally developed by the Open Physics Project (Tracker). Optical tracking was used to eliminate any potential error in the LVDT displacement measurement introduced due to compliance of the test frame or slippage of the specimen in the grips. Post-test analysis of the samples showed some signs of slip in the grip, particularly of the Al-Si intermetallic coating on the UHSS specimens. The fracture time of each video was synchronized with the large drop in force measured by the load cell at failure. The zero time of the test video was then synchronized to the corresponding time in the force response.

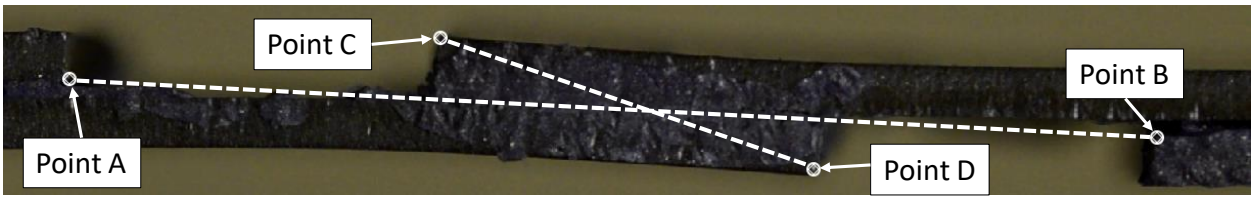

Figure 2: Location of tracked points from test video

2.2 Modeling techniques

Models of the tests were created (Figure 3a) and analyzed using a commercial finite element code (LS-DYNA R7.1.2 MPP double precision). A 3-dimensional analysis using non-linear geometry was carried out to avoid any potential difficulties that may be observed with mismatched out-of-plane response due to differing Poisson's ratios of the three metal adherends, though to reduce the computational resources needed to run these models, a reflected (symmetry) boundary condition was applied along the long axis of the model. Shell elements were used to model the adherends due to their ability to capture bending response properly with a single element through thickness and their extensive use when modeling vehicle bodies-in-white during crash simulations.

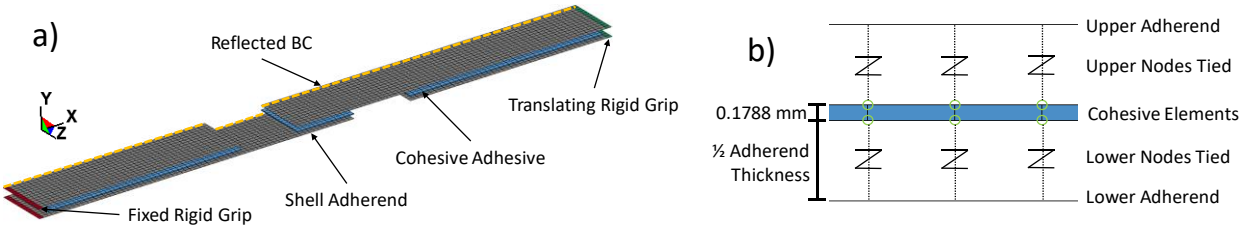

Figure 3: Lap shear model (a) with detailed schematic of bond line (b)

The adherends were meshed with 1 mm x 1 mm fully-integrated Reissner-Mindlin shell elements with assumed strain interpolation to treat in-plane bending behavior and 7 integration points through thickness as described by Halquist [15]. The portion of the sample inside the grips was assumed to be rigidly connected to the grips, which were modeled as a single row of rigid elements on either end of the sample, 127 mm apart, as in the experiments. The grips used to test the samples were pin jointed at their attachment to the test machine, allowing translation perpendicular to the long axis of the test specimen. To model this end condition, the axial displacement of the model was fixed at one end and a constant velocity of 1.78 mm/s was prescribed to the other end along the axial direction of the sample, with all other degrees of motion being free. To ensure that the models represented a quasi-static response, the kinetic energy for each simulation was monitored and found to be negligible (<1% of the internal energy at failure). The thickness of the shell elements was set according to the thickness measured for each adherend (1.8 mm for steel and 1.65 mm for aluminum and magnesium) and the midplane of each set of shells was positioned accordingly. The overlap of the model of each test condition was set to the average measured for each adherend combination (Table 1). This allowed for a more direct comparison between the model and average test force data.

Table 1: Bond line length

	Measured Joint Overlap [mm]			
Adherend Combination	Test 1	Test 2	Test 3	Average
UHSS-UHSS	15.5	13.5	16.0	15.0
AA5182-AA5182	13.5	13.5	12.0	13.0
ZEK 100-ZEK 100	12.0	12.0	11.5	11.8
UHSS-AA5182	11.0	13.0	14.0	12.7
UHSS-ZEK 100	14.0	12.0	12.0	12.7
AA5182-ZEK 100	13.0	14.0	15.0	14.0

Each of the three adherend materials was modeled using a piecewise linear plasticity model. The material models were based on parameter fitting described by Bardelcik *et al.* [16], Smerd *et al.* [17], and Kurukuri *et al.* [18] for the steel, aluminum, and magnesium, respectively. In each of these studies, strain rate dependent material properties were fit to power law fits across a range of loading rates. The current study has assumed constant quasi-static loading for all cases to simplify the analysis. The UHSS material fit also assumed a constant Vickers hardness of 460 HV, the highest that was measured experimentally using a 1 kgf indenter load as described by Omer *et al*. [14]. The rolling direction and transverse direction properties were averaged for the magnesium adherend models as the tested adherends were of indeterminate orientation. The elastic properties (Table 2) and flow stress of the three materials (Figure 4), highlight a significant difference in response of the high strength steel compared to the other materials, which have similar flow stress response, though there is some difference in their elastic properties. Failure was not considered in the adherend material models since no adherend failure occurred during the testing.

Table 2: Elastic properties of adherends

	Steel	Aluminum	Magnesium
Density [kg/m³]	7.8	2.7	1.6
Young's Modulus [GPa]	200	70	45
Poisson's Ratio	0.30	0.33	0.35

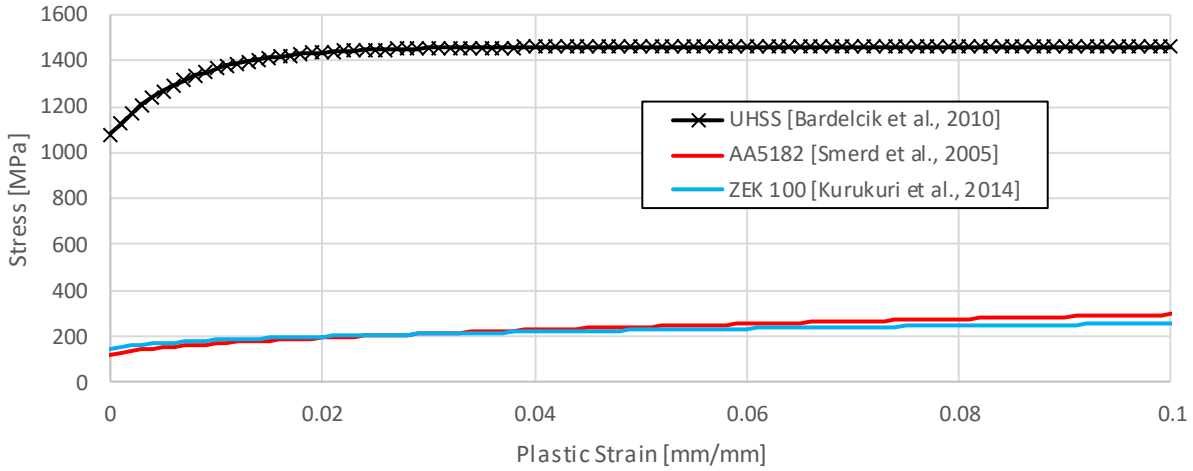

Figure 4: Hardening response of the adherend material models

The adhesive was modeled using eight-node, finite thickness cohesive (CZM) elements, which are often used to model the interface between continuum elements commonly used in finite element modeling. These elements are defined in such a way that the displacement of the top surface and bottom surface can be tracked throughout the simulation. Cohesive elements use special constitutive models that describe the tensile (Mode I) and shear (Mode II) traction-separation (stress-displacement) response of the material with a simplified representation of these responses. These traction-separation responses are often bilinear or trapezoidal relationships, with the area under the traction-separation responses being associated with the energy required to create a new surface within the adhesive, the energy release rate. The displacement in the normal direction (Mode I) and transverse direction (Mode II) are tracked independently, meaning that no Poisson's effects are considered. The final failure of each element is often described using a failure criterion that relates the Mode I and Mode II energy release rates to their critical values (*i.e.* pure Mode I or Mode II response). A more detailed description of the use of cohesive elements in finite element modeling is described by Da Silva & Campilho [19]. In the current study, 1 mm x 1 mm cohesive elements were used to model the adhesive, with a thickness of 0.18 mm to match the bond line thickness used in the test (Figure 3b). This mesh size was chosen after a mesh refinement study to ensure a reasonable number of elements ahead of the crack front would be in the damaged region of the traction separation response. The top and bottom surfaces of the cohesive elements were then tied to their respective shell midplanes using an offset constraint that accounted for the transfer of moment to the shell (*CONTACT_TIED_SHELL_EDGE_TO_SURFACE_CONSTRAINED_OFFSET in LS-DYNA). The SA9850 adhesive response was modeled using a trapezoidal traction-separation cohesive zone model, with parameters originally defined by Trimiño & Cronin [20] (Figure 5a). The constitutive model was originally developed to include rate sensitivity of the peak traction in both Mode I and Mode II loading using bulk material samples. As with the adherend material, the material parameters (Table 3) at a single rate were selected corresponding to the nominal test strain rate (1 s^{-1}) to simplify the analysis.

Table 3: Cohesive material properties of SA9850 adhesive

Loading Direction	Stiffness (E_I, E_{II}) [MPa/mm]	Peak Traction (S_I, S_{II}) [MPa]	Critical Energy Release Rate ($G_{I,C}$, $G_{II,C}$) [kJ/mm²]	Ratio of Area Under Plateau to Critical Energy Release Rate (f_{GI}, f_{GII})
Mode I	2490	46.75	2.97	0.7
Mode II	850	25.53	15	0.78

Under mixed mode loading, the separation corresponding to the plateau stress (*i.e.* the end of the initial linear response of the traction-separation response) was defined by:

$$\left(\frac{\delta_I}{S_I/E_I}\right)^2 + \left(\frac{\delta_{II}}{S_{II}/E_{II}}\right)^2 = 1$$

Where δ_I and δ_{II} are the separation in the Mode I and Mode II directions under mixed mode loading, respectively, S_I and S_{II} are the peak traction in Mode I and Mode II, and E_I and E_{II} are the initial stiffness of the CZM in Mode I and Mode II.

Similarly, the separation at damage initiation (the end of the plateau region of the traction-separation response) was defined as:

$$\left(\frac{\delta_I}{S_I/E_I + f_{GI}\cdot G_{I,C}/S_I}\right)^2 + \left(\frac{\delta_{II}}{S_{II}/E_{II} + f_{GII}\cdot G_{II,C}/S_{II}}\right)^2 = 1$$

Where f_{GI} and f_{GII} are the ratio of the area under the plateau stress to the total area under the traction-separation response in Mode I and Mode II and $G_{I,C}$ and $G_{II,C}$ were the total critical energy release rates defined for Mode I and Mode II, respectively.

Failure in the cohesive elements was defined by:

$$\frac{G_I^*}{G_{I,C}} + \frac{G_{II}^*}{G_{II,C}} = 1$$

Where G_I^* and G_{II}^* were the calculated energy release rates for a given loading angle for Mode I and Mode II respectively as described by Yang & Thouless [21]. The pure Mode I and Mode II responses (Figure 5b), were thus sufficient with this cohesive zone model to characterize the mode-mixity angle-resultant failure displacement response (Figure 5c).

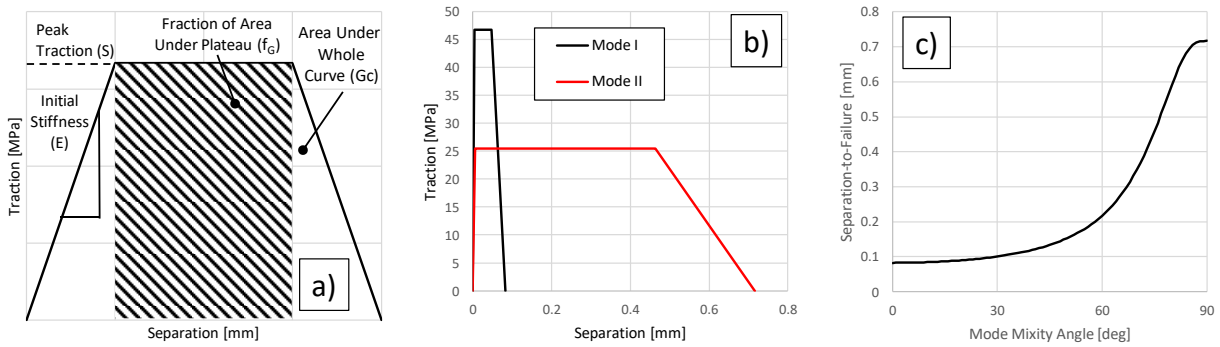

Figure 5: Parameters to create trapezoidal traction-separation response (a), pure Mode I and Mode II response (b) and mixed-mode resultant displacement to failure (c) of the cohesive model

3 Results and Discussion

The maximum nominal failure stresses (Table 4, Figure 6), calculated by dividing the failure force by the bonded area of each sample, were considerably higher for the UHSS-UHSS combination of adherends than for any other combination tested, with an average failure stress of 27.2 MPa. Other combinations had average failure stresses between 17.9 MPa and 23.9 MPa.

Table 4: Measured failure stress

	Nominal Failure Stress [MPa]			
Adherend Combination	Test 1	Test 2	Test 3	Average
UHSS-UHSS	27.67	26.50	27.47	27.22
AA5182-AA5182	21.97	21.70	22.59	22.09
ZEK 100-ZEK 100	21.97	23.56	20.54	22.02
UHSS-AA5182	23.30	23.61	15.64	20.85
UHSS-ZEK 100	23.76	25.68	22.26	23.90
AA5182-ZEK 100	17.45	19.14	17.24	17.94

While nominal failure stress (Figure 6) is a convenient method to normalize the failure force for samples that do not have the same overlap lengths, care must be taken not to overstate the ability of this measure to characterize the strength of the adhesive joint. Nonetheless, it is evident that in some cases the adherend material being bonded had a very strong effect on the failure stress. The nominal failure stress of each adherend combination was compared individually to each of the other combinations using a series of standard t-tests (assuming equal variance and a 2-sided normal distribution of response). The UHSS-UHSS and AA5182-ZEK 100 combinations exhibited statistically significant different average failure stresses to the other combinations (*i.e.* $p < 5\%$) except when compared to the UHSS-AA5182 combination that exhibited higher variability in failure stress relative to all other adherend combinations. No other pairs of adherend combinations exhibited a statistically significant difference in failure stress. One can

infer then, that the UHSS-UHSS is likely to exhibit higher joint strength, and the AA5182-ZEK 100 combination is likely to exhibit lower joint strength compared to the other test combinations.

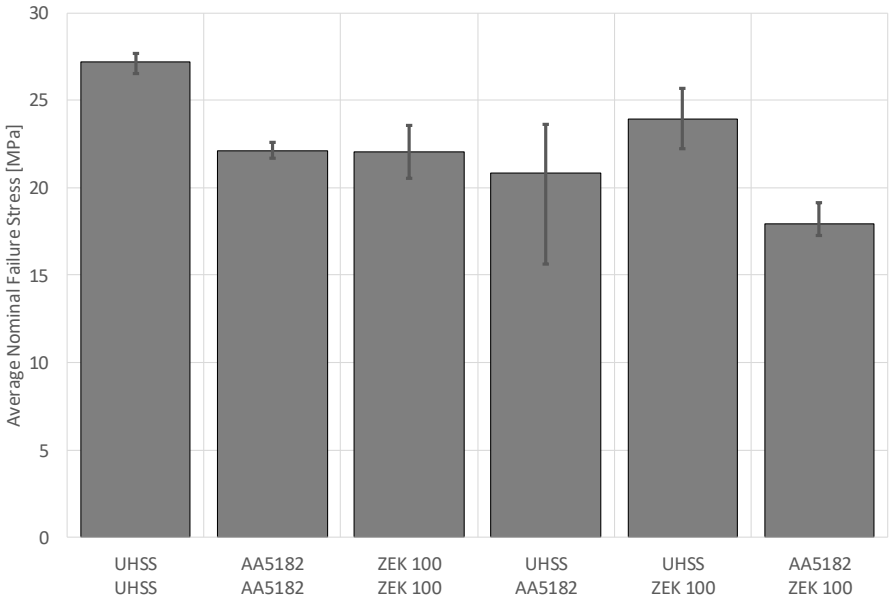

Figure 6: Average nominal shear stress at failure for each adherend-adhesive combination and test maximum and minimum

The typical failure surface for each combination (Figure 7) provided further insight into the measured response. For all UHSS and aluminum adherends, complete adhesive coverage remained on the fracture surfaces indicating a cohesive failure. Despite undergoing the same surface treatment as the other adherends, the ZEK 100 adherends exhibited mixed (cohesive/adhesive) failure with the leading edge of the lap joint failing cohesively (*i.e.* failure within the adhesive rather than at the interface), switching to adhesive or interfacial failure further along the bond line. Area measurements were carried out on the magnesium fracture surfaces using an opto-digital microscope and measurement system (Keyence VHX-5000). For the ZEK 100-ZEK 100 condition, an average of 66% adhesive coverage of the fracture surface was measured. For the UHSS-ZEK 100 combination this value was 56%, while for the AA5182-ZEK 100 combination, 39% adhesive coverage remained after fracture. Despite the partial interfacial failure present in the ZEK 100-ZEK 100 and UHSS-ZEK 100 combinations, these combinations did not exhibit a significant change in strength when compared to other conditions where fully cohesive failure was present, notably the AA5182-AA5182 and UHSS-AA5182 combinations. A significant difference in strength was only noted in the AA5182-ZEK 100 case, in which roughly 60% of the magnesium surface exhibited interfacial failure. While the focus of this work was to create samples with minimal surface treatment to simulate a low-cost surface preparation for use in mass production environments, further investigation into more advanced surface treatments could potentially suppress interfacial failure for all adherends.

UHSS UHSS	AA5182 AA5182	ZEK 100 ZEK 100	UHSS AA5182	UHSS ZEK 100	AA5182 ZEK 100
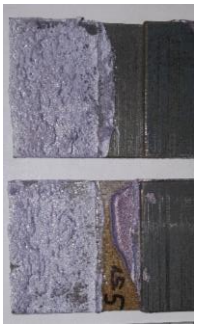	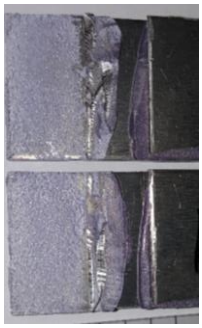		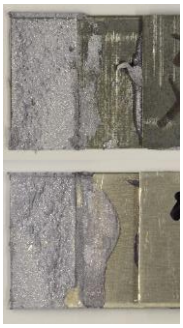	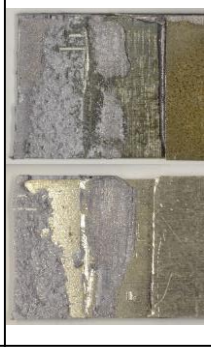	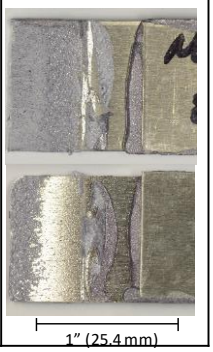

Figure 7: Failure surface of lap shear samples

A comparison of the force-displacement response generated when using the LVDT measured data and displacement obtained using the tracking methodology of this study presented in section 2.1 (Figure 8), highlighted the importance of the selection of displacement data used to compare to the model. The LVDT-measured displacement to failure was considerably larger (3 mm to 1.3 mm) than the tracked displacement (1.2 mm to 0.6 mm). For the samples in which only AA5182 and ZEK 100 adherends were used, the ratio between tracked displacement to failure and LVDT measured displacement to failure averaged 0.46 while this value was reduced to 0.32 for cases in which UHSS was used. The difference between these ratios highlighted the effect of the grip slipping on the intermetallic surface coating of the UHSS adherends. The effect of this slippage could be clearly seen in the nonlinear shape of the LVDT measured force-displacement response. Additional differences, caused by compliance in the test machine and the use of pin jointed wedge grips, were on the same order of magnitude or larger than the displacement to failure measured in this study. Due to the difficulty in interpreting the LVDT displacement measurements, the tracked displacement measurements were used for comparison to the model which, when combined with the measured joint rotation, provided a more meaningful comparison of the local kinematics of the joint than the cross-head (LVDT) measurements.

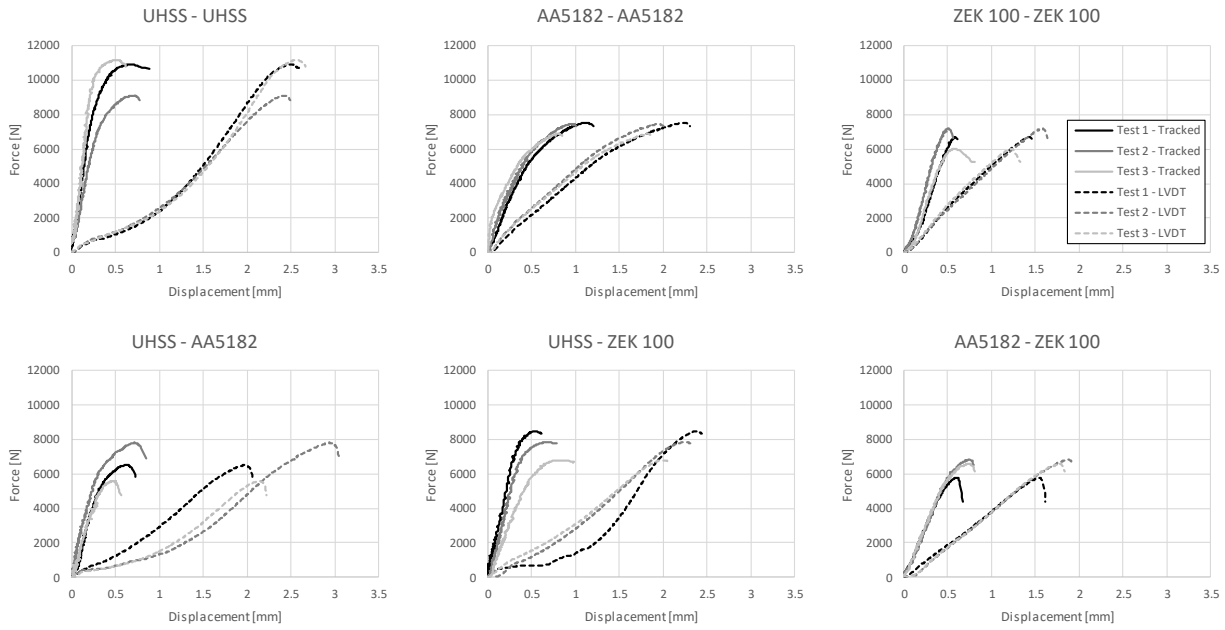

Figure 8: Comparison of force-displacement response using tracked and LVDT measured displacement

A comparison of the predicted and measured force-displacement (Figure 9) and displacement-rotation (Figure 10) showed the model captured the response of the tests across most adherend combinations. The peak predicted force generally coincided with the onset of damage in the adhesive, followed by a rapid reduction in joint force. Ultimate failure of the joint occurred rapidly after the first CZM element reached zero traction. For the cases in which there was significant plastic deformation in both adherends (e.g. aluminum), the model tended to overpredict the displacement to failure, while in conditions involving the UHSS adherend, which exhibited no plastic deformation, the model tended to underpredict the displacement to failure. The variability in measured maximum force and initial slope was higher in the tests with UHSS adherends compared to the aluminum or magnesium materials. While the lower stiffness and strength adherends plastically deformed at lower loads, the lack of deformation in the UHSS material potentially led to greater sensitivity to variability in bond line thickness and initial joint geometry. Additionally, the samples made using UHSS exhibited more variability in the bond line length than was present in the other combinations, which may also account for some of the variability in test response.

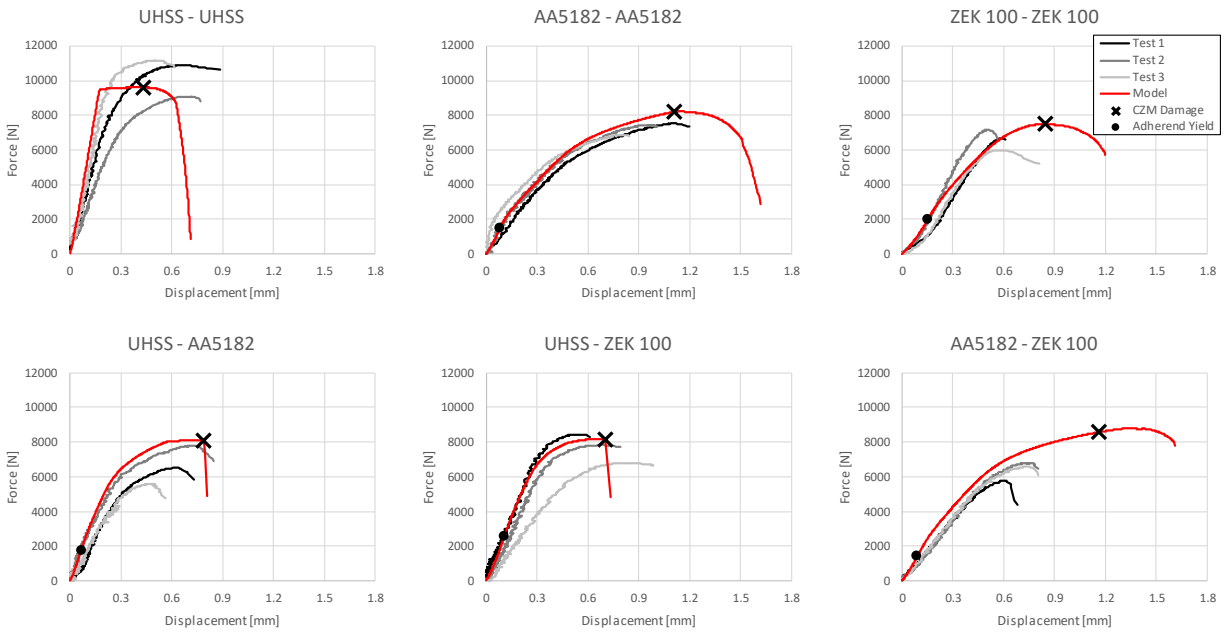

Figure 9: Model and test force-displacement response

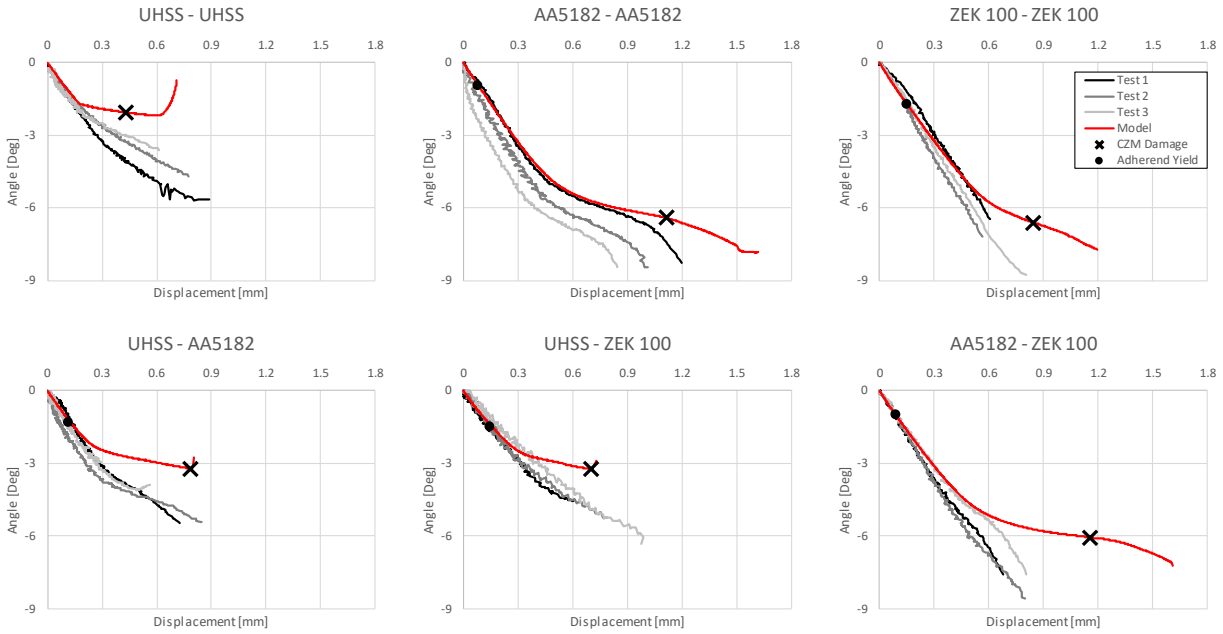

Figure 10: Model and test joint rotation-displacement response

The bulk material tests used to develop the CZM used in this study lacked the confinement present in bonded sample test geometry. In particular, the G_{IIC} value (15 kJ /mm^2) is considerably higher than would be expected in bonded samples, which for typical toughened adhesive may be roughly 2 times the value of G_{IC} as noted by Mall [22]. Using a lower value of G_{IIC} would generally reduce the displacement-to-failure,

however the intent with this work was to use previously published material data rather than generating material properties *via* inverse modeling. In general, the current modelling approach was able to reasonably capture test response when plastic deformation was present in the adherends, but also highlights the importance of the adherend material properties and geometry on the overall joint response.

The UHSS response highlighted the need for further detail in the CZM necessary to model these joints. The commonly used trapezoidal traction-separation response includes a sharp transition from the linear to plateau response (Figure 5). The model reaches a force equilibrium when elements in the adhesive reach this sharp corner in the traction-separation response. At this point, the force necessary to bend the adherend further is equal to the force necessary to deform the adhesive. The resulting force-displacement response of the test specimen correspondingly exhibits a plateau response, due to the plateau region in the adhesive traction-separation curve. The plateau assumption of the traction-separation response is also manifest in the joint rotation measure, where the rotation essentially stops once the CZM elements reach the stress plateau and the adhesive layer is stretched at constant force until damage initiation, explaining the under-prediction of rotation response for tests with UHSS adherends.

In the models, elements at the leading edge of the bond line in samples which exhibited plastic deformation demonstrated a higher amount of Mode I loading due to the bending of the adherends, as also seen in the test responses. Additionally, a 'plastic hinge', which occurs when the portion of the adherend far from the bonded region remains relatively undeformed leading to a concentration of bending strain immediately adjacent to the bond line as described by Kafkalidis & Thouless [11], was present in the adherends which deformed plastically. To empirically assess the effect of mode-mixity at an elemental level in each model, the Mode I and Mode II energy release rates of the element at the middle of the leading edge of bond line were calculated by the integrating the element traction with respect to separation for both Mode I and Mode II. These elements were among the first to fail in each simulation, and so could be thought of as the critical elements which governed the initiation of failure of the bond area. The energy release rates were normalized by dividing by the respective critical energy release rate in pure Mode I and pure Mode II loading. The normalized energy release rate-displacement response (Figure 11), showed that in conditions in which both sides of the joint plastically deformed, the Mode I response tended to be a larger contributor to the joint failure, whereas when little bending was present (the UHSS-UHSS combination), Mode II dominated. The multi-material combinations involving UHSS showed an almost equal share of the loading modes, though the onset of failure occurred very abruptly near the ultimate failure displacement, whereas the other conditions tended to be more gradual. Due to the failure criterion used in these models, the sum of the Mode I and Mode II response should equal unity at failure, if the element was loaded at a constant mode-mixity angle. Because the mode-mixity was changing throughout the simulation, the sum of the normalized Mode I and Mode II energy release rates at failure was not, in general, equal to unity.

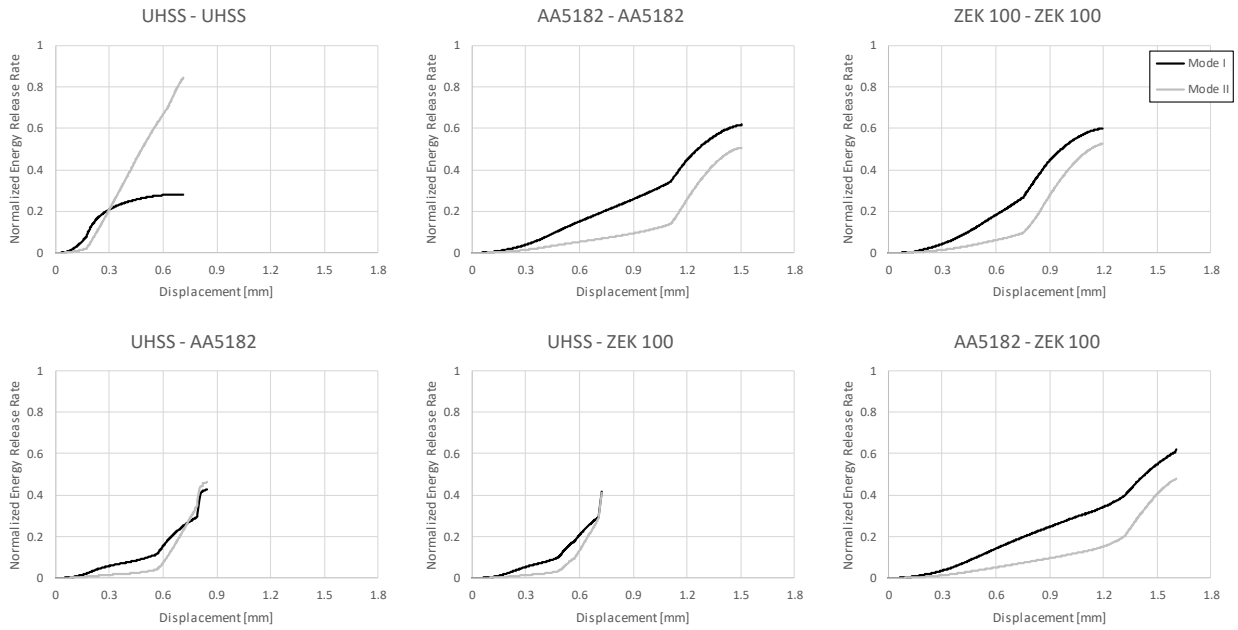

Figure 11: Normalized energy release rates of critical elements in Mode I and Mode II

The current modeling methodology did not account for the interfacial failure that was observed in a number of tests involving ZEK 100. This was particularly pronounced in the AA5182-ZEK 100 tests in which a substantial portion of the failure surface exhibited interfacial failure. This was manifest in the displacement to failure and peak force; the model predicted these values being considerably higher than the test data for this condition, presumably since interfacial failure occurs prior to onset of cohesive failure for the current ZEK100 substrate and surface preparation. Since a key aspect of the current work was to examine whether failure of the adhesive could be predicted based on CZM properties determined from on bulk adhesive testing, the introduction of adhesive failure calibration was considered beyond the scope of the current work.

The results from this study highlight several important considerations when using adhesive bonding in multi-material metallic structures. It is critical to understand the implications of different material choices on the load sharing across a given joint. Even with the very straightforward and well-controlled loading conditions applied to the simple geometry in this study, different responses were seen depending on relatively small changes in the orientation of the joint at failure. When considering the potentially large number of loading modes in an automotive crash environment, in which changes in impact velocity, mass or principal direction of impact can drastically alter the load path through a crash structure, the necessity to consider a wide range of loading conditions when designing an adhesive joint becomes apparent.

4 Conclusions

Testing of multi-material metallic single lap shear joints revealed that the adherend material selection had a strong effect on the peak force that could be transmitted through the joint. Of the materials tested, the samples that included AA5182 and ZEK 100 (which exhibit similar plastic response) had similar failure

strengths between 23.9 MPa to 17.94 MPa (21.4 MPa average), while a statistically significant increase in strength was observed when UHSS was used on both sides of the joint (27.2 MPa). Additionally, the strength of the AA5182-ZEK 100 combination was significantly lower than the remaining combinations due to a higher propensity of this combination to exhibit interfacial failure.

The intention of this study was to emulate a large-scale production environment with minimal surface preparation carried out; however testing of the adherend materials in the as-received state resulted in partial interfacial failure, particularly with the ZEK 100 magnesium material. For the same surface treatment, some adherends demonstrated cohesive failure while others exhibited interfacial failure, highlighting the importance of surface preparation to achieve cohesive failure.

The modeling methodology used in this study comprising a CZM adhesive connected with a tied contact to adherends modeled with shell elements was shown to predict the force, displacement and joint rotation response of the tested adherend combinations (average R^2 of 0.86), using material data for the adhesive and adherends from the open literature. The current modeling methodology was used to explain the differences seen in the test response by examining the mode-mixity of the adhesive at the root of the bond line. For bonds involving AA5182 and ZEK 100 adherends, the normalized energy release rate from Mode I and Mode II loading was roughly equal in the region of the bonded area where failure initiated. The higher stiffness and yield strength of the UHSS adherends reduced bending, which in turn led to an increase in Mode II loading within the joint. The normalized energy release rate in Mode II was 80% at failure compared to 53% to 41% for other joints. The higher proportion of Mode II loading for higher stiffness and higher strength adherends increased the overall joint strength. An advantage of the current methodology is the ability to scale for use in current state of the practice crash models by using a computationally efficient approach while still providing a fully three-dimensional analysis.

Acknowledgements: The authors would like to express their thanks to Honda Research and Development Americas, 3M Canada Company, ArcelorMittal, Compute Canada, Ontario Centers of Excellence and the Natural Sciences and Engineering Research Council of Canada (NSERC) for their support of this research.

5 References

1. Mayyas A, Shen Q, Mayyas A, Shan D, Qattawi A, Omar M. Using quality function deployment and analytical hierarchy process for material selection of body-in-white. Mater & Des 2011;32(5):2771-2782. doi: https://doi.org/10.1016/j.matdes.2011.01.001

2. Conklin J, Beals R, Brown Z. BIW Design and CAE. SAE Technical Paper 2015;2015-01-0408. Presented at the SAE 2015 World Congress & Exhibition, Detroit, USA, April 21-23, 2015. doi: https://doi.org/10.4271/2015-01-0408

3. Peroni L, Avalle M, Belingardi G. Comparison of the energy absorption capability of crash boxes assembled by spot-weld and continuous joining techniques. Int J Impact Eng 2009;36(3):498-511. doi: https://doi.org/10.1016/j.ijimpeng.2008.06.004

4. Meschut G, Janzen V, Olfermann T. Innovative and highly productive joining technologies for multi-material lightweight car body structures. J Mater Eng Perform 2014;23(5):1515-1523. doi: https://doi.org/10.1007/s11665-014-0962-3

5. Gonçalves JPM, De Moura MFSF, De Castro PMST. A three-dimensional finite element model for stress analysis of adhesive joints. Int J Adhes Adhes 2002;22(5):357-365. doi: https://doi.org/10.1016/S0143-7496(02)00015-5

6. Matsuyama S, Yamashita H. Development of Smart Design Process for Light Weight Body in White. SAE Int J Mat Manuf 2015;8:554-562. doi: https://doi.org/10.4271/2015-01-1365

7. Banea MD, Rosioara M, Carbas RJC, da Silva LFM. Multi-material adhesive joints for automotive industry. Compos Part B: Eng 2018;151:71-77. doi: https://doi.org/10.1016/j.compositesb.2018.06.009

8. Hua Y, Gu L, Trogdon M. Three-dimensional modeling of carbon/epoxy to titanium single-lap joints with variable adhesive recess length. Int J Adhes Adhes 2012;38:25-30. doi: https://doi.org/10.1016/j.ijadhadh.2012.06.003

9. Avendano R, Carbas RJC, Marques EAS, da Silva LFM, Fernandes AA. Effect of temperature and strain rate on single lap joints with dissimilar lightweight adherends bonded with an acrylic adhesive. Compos Struct 2016;152:34-44. doi: https://doi.org/10.1016/j.compstruct.2016.05.034

10. Ghosh D, Pancholi L, Sathaye A. Comparative Studies of Adhesive Joints in Automotive. SAE Technical Paper 2014;2014-01-0788. Presented at the SAE 2014 World Congress & Exhibition, Detroit, USA, April 8-10, 2014. doi: https://doi.org/10.4271/2014-01-0788

11. Kafkalidis MS, Thouless MD. The effects of geometry and material properties on the fracture of single lap-shear joints. Int J Solids Struct 2002;39(17):4367-4383. doi: https://doi.org/10.1016/S0020-7683(02)00344-X

12. Guess TR, Allred RE, Gerstle FP. Comparison of lap shear test specimens. J Test Eval 1977;5(2):84-93. doi: https://doi.org/10.1520/JTE10666J

13. Richardson G, Crocombe AD, Smith PA. A comparison of two-and three-dimensional finite element analyses of adhesive joints. Int J Adhes Adhes 1993;13(3):193-200. doi: https://doi.org/10.1016/0143-7496(93)90042-8

14. Omer K, George R, Bardelcik A, Worswick M, Malcolm S, Detwiler D. Development of a hot stamped channel section with axially tailored properties-experiments and models. Int J Mater Forming 2017;11(1):149-164. doi: https://doi.org/10.1007/s12289-017-1338-7

15. Halquist J. LS-DYNA Theory Manual: Chapter 11 - Fully Integrated Shell (Type 16). Livermore, Ca: Livermore Software Technology Corporation; 2017. Available on-line: http://ftp.lstc.com/anonymous/outgoing/jday/manuals/DRAFT_Theory.pdf. Accessed February 27, 2019.

16. Bardelcik A, Worswick MJ, Winkler S, Wells MA. A strain rate sensitive constitutive model for quenched boron steel with tailored properties. Int J Impact Eng 2012;50:49-62. doi: https://doi.org/10.1016/j.ijimpeng.2012.06.007

17. Smerd R, Winkler S, Salisbury C, Worswick M, Lloyd D, Finn M. High strain rate tensile testing of automotive aluminum alloy sheet. Int J Impact Eng 2005;32(1):541-560. doi: https://doi.org/10.1016/j.ijimpeng.2005.04.013

18. Kurukuri S, Worswick MJ, Bardelcik A, Mishra RK, Carter JT. Constitutive behavior of commercial grade ZEK100 magnesium alloy sheet over a wide range of strain rates. Metall Mater Trans A 2014;45(8):3321-3337. doi: https://doi.org/10.1007/s11661-014-2300-7

19. Da Silva L F, Campilho RD. Advances in numerical modelling of adhesive joints. Heidelberg: Springer; 2012. doi: https://doi.org/10.1007/978-3-642-23608-2

20. Trimiño LF, Cronin DS. Evaluation of Numerical Methods to Model Structural Adhesive Response and Failure in Tension and Shear Loading. J Dyn BehavMater 2016;2:122-37. doi: https://doi.org/10.1007/s40870-016-0045-7

21. Yang QD, Thouless MD. Mixed-mode fracture analyses of plastically-deforming adhesive joints. Int J Fract 2001;110(2);175-187. doi: https://doi.org/10.1023/A:1010869706996

22. Mall S. Influence of resin on delamination. In Delamination Behaviour of Composites. Cambridge: Woodhead Publishing; 2008;721-740. doi: https://doi.org/10.1533/9781845694821.5.721